Pore-scale simulation of H_2-brine system relevant for underground hydrogen storage
A lattice Boltzmann investigation

Wang, Yuhang; Chakrapani, Thejas Hulikal; Wen, Zhang; Hajibeygi, Hadi

DOI
10.1016/j.advwatres.2024.104756

Publication date
2024

Document Version
Final published version

Published in
Advances in Water Resources

Citation (APA)
Wang, Y., Chakrapani, T. H., Wen, Z., & Hajibeygi, H. (2024). Pore-scale simulation of H_2-brine system relevant for underground hydrogen storage: A lattice Boltzmann investigation. *Advances in Water Resources*, *190*, Article 104756. https://doi.org/10.1016/j.advwatres.2024.104756

Advances in Water Resources 190 (2024) 104756

Contents lists available at ScienceDirect

Advances in Water Resources

journal homepage: www.elsevier.com/locate/advwatres

Pore-scale simulation of H_2-brine system relevant for underground hydrogen storage: A lattice Boltzmann investigation

Yuhang Wang [a,*], Thejas Hulikal Chakrapani [b], Zhang Wen [a], Hadi Hajibeygi [b]

[a] School of Environmental Studies, China University of Geosciences, Wuhan, 430078, China
[b] Faculty of Civil Engineering and Geosciences, Department of Geoscience and Engineering, Delft University of Technology, Delft, 2628CV, The Netherlands

ARTICLE INFO

Keywords:
Underground hydrogen storage
Flow in porous media
Pore-scale modeling
Relative permeability

ABSTRACT

Underground hydrogen (H_2) storage in saline aquifers is a viable solution for large-scale H_2 storage. Due to its remarkably low viscosity and density, the flow of H_2 within saline aquifers exhibits strong instability, which needs to be thoroughly investigated to ensure safe operations at the storage site. For the first time, we develop a lattice Boltzmann model tailored for pore-scale simulations of the H_2-brine system under typical subsurface storage conditions. The model captures the significant contrast of fluid properties between H_2 and brine, and it offers the flexibility to adjust the contact angle to suit varying wetting conditions. We show that the snap-off is enhanced in a system with a high capillary number and a small contact angle. These conditions lead to a low recovery factor, which is unfavorable for H_2 production from the aquifer. Moreover, the relative permeability curves, computed from the simulation results, exhibit distinct behaviors for H_2 and brine. In the case of the wetting phase, the relative permeability can be quantified using the quadratic expression, whereas for the non-wetting phase, the relative permeability exhibits a nearly linear behavior, and saturation alone appears insufficient to characterize the relative permeability at large saturations of non-wetting phase. This implies that different formula for liquid and gas phases may be employed for continuum-scale simulations.

1. Introduction

Underground hydrogen storage (UHS) has emerged as a promising strategy to effectively address the intermittency nature of renewable energy within a zero-carbon energy economy (Gahleitner, 2013; Tarkowski, 2019; Hematpur et al., 2023; Krevor et al., 2023). By utilizing the ample volume offered by geological formations, UHS enables the storage of H_2 at significant capacities for extended durations (Lord et al., 2014; Heinemann et al., 2021; Zivar et al., 2021). Three major geological structures are considered for UHS: salt caverns, depleted gas reservoirs, and saline aquifers. Among these options, UHS in saline aquifers exhibits the most intricate flow behavior as it involves multiphase flow with a large contrast of fluid properties.

The migration and distribution of H_2 in the saline aquifer depend on the interactions of H_2, brine and rock. These interactions can be characterized using pore-scale parameters, i.e., interfacial tension and contact angle. Experimental studies have been conducted to measure the contact angle for the H_2-brine system, and hydrophilic wetting conditions are consistently observed (Yekta et al., 2018; Hashemi et al., 2021b; Iglauer et al., 2021; Higgs et al., 2022; van Rooijen et al., 2022). The contact angle is higher in rock samples with higher concentrations of organic materials in their composition. Furthermore, the static contact angle remains unaffected by various physical parameters such as pressure, temperature and salinity. However, the interfacial tension exhibits a negative/positive linear relation with temperature and salinity, respectively (Hosseini et al., 2022).

With the measured pore-scale parameters, one can perform numerical simulations to predict the dynamics of flow for the H_2-brine system at pore-scale, and further derive constitutive relations, i.e., relative permeability and capillary pressure, which are indispensable for field-scale predictions (Pfeiffer and Bauer, 2015; Luboń and Tarkowski, 2020; Eller et al., 2022; Bo et al., 2023; Chai et al., 2023; Pan et al., 2023; Zhao et al., 2023). Traditionally, constitutive relations are measured from core-flood experiments (Yekta et al., 2018; Boon and Hajibeygi, 2022), which can be time-consuming and expensive (Berg et al., 2016; Blunt, 2017). Pore-scale simulation techniques have emerged as efficient alternatives to predict multiphase flow parameters. These methods can be classified into two main categories: pore network modeling (PNM) and computational fluid dynamics (CFD) method (Meakin and Tartakovsky, 2009; Joekar-Niasar and Hassanizadeh, 2012). In PNM,

---

[*] Corresponding author.

E-mail addresses: wangyuhang17@cug.edu.cn (Y. Wang), t.hulikalchakrapani@tudelft.nl (T.H. Chakrapani), wenz@cug.edu.cn (Z. Wen), h.hajibeygi@tudelft.nl (H. Hajibeygi).

https://doi.org/10.1016/j.advwatres.2024.104756
Received 23 February 2024; Received in revised form 21 May 2024; Accepted 14 June 2024

the simulation is performed based on a pore network extracted from the pore space of a rock sample, where larger pore volumes are represented by interconnected pores linked through throats (Piri and Blunt, 2005; Blunt, 2017). CFD simulations are conducted in a more explicit manner by using the pore structure obtained from either experimental characterization or numerical reconstruction directly. Traditional CFD methods, such as the volume-of-fluid (Raeini et al., 2012) or the level-set (Prodanović and Bryant, 2006) ones, are established based on the Navier–Stokes equations. These methods rely on the use of an auxiliary algorithm to track the movement of the interface besides solving flow equations. The lattice Boltzmann method (LBM), alternatively, describes multiphase flow using a more fundamental Boltzmann equation, which captures the essential physics at mesoscopic level without incorporating molecular interactions explicitly. Compared to the traditional methods, LBM offers compelling advantages. Firstly, LBM is inherently parallelizable, allowing for efficient computation on parallel computing architectures. Secondly, LBM simplifies the handling of complex geometries and boundary conditions, making it well-suited for simulating flow in porous media with nontrivial fluid–fluid and fluid-solid interactions (Huang et al., 2009; Ramstad et al., 2012; Chen et al., 2014).

Different LBM models have been developed to simulate multiphase flow, including the pseudopotential model (Shan and Chen, 1993), the color-gradient model (Gunstensen et al., 1991), the free-energy model (Swift et al., 1995), and the mean-field theory model (He et al., 1999). Notably, the first two models are widely used for two-phase flow problems in porous media. One of the major limitations encountered by those two models is the numerical instability, which arises in systems exhibiting a substantial contrast of physical properties, such as density and viscosity between the two fluids (Liu et al., 2016). Efforts have been made to address this limitation; however, they may compromise the simplicity of LBM and results in increased computational costs (Chen et al., 2014). This work focuses on the application of the pseudopotential model, in which the separation of phases is achieved automatically via interparticle forces. Additionally, it provides the flexibility to incorporate different forms of equation of state (EOS). In contrast to the previous works that utilized cubic EOS for pore-scale simulations (Huang et al., 2009; Son et al., 2016; Liu et al., 2021; Qin et al., 2021; Zhang et al., 2022), a piece-wise linear EOS (Colosqui et al., 2012) is selected to manage the fluids with significant contrast in their physical properties.

Due to the potential numerical instability, few works have investigated H_2-brine system using pore-scale simulation techniques. Hashemi et al. (2021a) used the quasi-static PNM to simulate fluid flow relevant for UHS, and quantified the relative permeability and capillary pressure, as well as their dependencies on wettability and rock types. Note that the quasi-static PNM is particularly suitable for the capillary-dominated flow regime (Valvatne and Blunt, 2004, Gong et al., 2021a,b). In other words, the capillary pressure acts as the primary driving force determining the evolution of fluid distribution. As a result, only the connected flow pathways are captured (Berg et al., 2016). However, pore-scale experiments have shown that the snap-off events, causing the H_2 to be disconnected and trapped, play an important role in the distribution of non-wetting phase (Jangda et al., 2023). This implies that both connected flow pathways and ganglion dynamics exist and should be accounted for in the model. Wang et al. (2023) employed the OpenFOAM platform to study the impact of wettability on the flow behavior of H_2-brine system. Results showed that the snap-off dominates the flow in both drainage (injection) and imbibition (reproduction) processes, which leads to a low recovery factor. To the best of our knowledge, there exists no detailed work in literature examining the H_2-brine system using LBM from a pore-scale perspective. As such, the primary objective of this work is to present a newly developed LBM model that is able to capture pore-scale dynamics of flow for H_2 and brine.

In the remainder of this paper, we first describe the governing equation for the single-component, multiphase (SCMP) pseudopotential LBM. The fluid–fluid and fluid–solid interactions are calculated using the pseudopotential functions, which are derived based on a piecewise linear EOS to achieve a robust numerical stability. We validate the developed model via (a) the static Laplace law, and (b) the dynamic capillary intrusion test. In both tests, the contrast of fluid properties are set such that it is representative for the UHS system. The developed model is then used to simulate two-phase flow of H_2 and brine in a synthetic porous medium at varying flow conditions. We quantify the relative permeabilities based on the simulation results, and further analyze the correlation between the relative permeability of each phase and state parameters. We close with a discussion of key findings and possible directions for future work.

2. Methods

2.1. Governing equation

We implement the pseudopotential LBM for a single-component, multiphase system. Two immiscible fluids, i.e., H_2 and brine, are described by a single set of distribution functions, with their respective physical properties defined independently. The evolution equation of the distribution function is given by (He and Luo, 1997)

$$f_\alpha\left(\mathbf{x}+\mathbf{e}_\alpha\delta t, t+\delta t\right) - f_\alpha\left(\mathbf{x}, t\right) = \Omega_\alpha\left(f\left(\mathbf{x}, t\right)\right) + \bar{F}_\alpha\left(\mathbf{x}, t\right), \tag{2.1}$$

where $f_\alpha(\mathbf{x}, t)$ is the distribution function along α-direction at time t and position vector $\mathbf{x}$, δt is the time step, and $\mathbf{e}_\alpha$ is a vector of discrete velocities. The two-dimensional, nine-velocity (D2Q9) lattice model is used, in which the discrete velocities are given by $\mathbf{e}_0 = (0, 0)$, $\mathbf{e}_1 = -\mathbf{e}_3 = (1, 0)$, $\mathbf{e}_2 = -\mathbf{e}_4 = (0, 1)$, $\mathbf{e}_5 = -\mathbf{e}_7 = (1, 1)$, and $\mathbf{e}_6 = -\mathbf{e}_8 = (-1, 1)$. $\Omega_\alpha\left(f\left(\mathbf{x}, t\right)\right)$ is the collision operator describing the rate of change of $f_\alpha\left(\mathbf{x}, t\right)$ resulting from collision, and $\bar{F}_\alpha\left(\mathbf{x}, t\right)$ is the forcing term accounting for external forces.

The MRT collision operator is given by (Lallemand and Luo, 2000; d'Humières, 2002)

$$\Omega_\alpha\left(f\right) = -\sum_\beta \left(\mathbf{M}^{-1}\mathbf{S}\mathbf{M}\right)_{\alpha\beta}\left(f_\beta - f_\beta^{\mathrm{eq}}\right), \tag{2.2}$$

where $\mathbf{M}$ is the transformation matrix that projects the distribution functions and their equilibrium ones onto the moment space, i.e., $\mathbf{m} = \mathbf{M}\mathbf{f}$ and $\mathbf{m}^{\mathrm{eq}} = \mathbf{M}\mathbf{f}^{\mathrm{eq}}$. $\mathbf{m}$ (and $\mathbf{m}^{\mathrm{eq}}$) denotes macroscopic physical quantities, namely,

$$\mathbf{m} = \left(\rho, e, \varepsilon, j_x, q_x, j_y, q_y, p_{xx}, p_{xy}\right)^T, \tag{2.3}$$

where ρ is density, e is internal energy, ε is the square of internal energy, j_x and j_y are the momentum in x and y directions, q_x and q_y are energy fluxes, and p_{xx} and p_{xy} are diagonal and off-diagonal components of the stress tensor. MRT operator allows different moments to relax at their own rates, which are stored in a diagonal matrix given by

$$\mathbf{S} = \mathrm{diag}\left(\tau_\rho, \tau_e, \tau_\varepsilon, \tau_j, \tau_q, \tau_j, \tau_q, \tau_s, \tau_s\right)^{-1}, \tag{2.4}$$

with τ_i denoting the relaxation time for the ith moment in Eq. (2.3). Values of τ_i are chosen as follows (Li et al., 2013; Zhao et al., 2019): $\tau_\rho = \tau_j = 1$, $\tau_e^{-1} = \tau_\varepsilon^{-1} = 0.51$, $\tau_q^{-1} = 1.1$, and τ_s is calculated via a linear interpolation given by (Mukherjee and Abraham, 2007)

$$\tau_s = \tau_V + \frac{\rho - \rho_V}{\rho_L - \rho_V}\left(\tau_L - \tau_V\right), \tag{2.5}$$

where ρ_L and ρ_V are the prescribed densities for liquid and vapor phases, respectively; τ_L and τ_V are relaxation times of pure phase, which are linked to the kinematic viscosity as $\nu = \left(\tau_s - 0.5\right) c_s^2 \delta t$ (c_s is the sound of speed). f_α^{eq} is the discrete equilibrium Maxwellian distribution function expressed by

$$f_\alpha^{\mathrm{eq}} = w_\alpha \rho \left[1 + \frac{\mathbf{e}_\alpha \cdot \mathbf{u}}{(c_s)^2} + \frac{(\mathbf{e}_\alpha \cdot \mathbf{u})^2}{2(c_s)^4} - \frac{\mathbf{u}\cdot\mathbf{u}}{2(c_s)^2}\right], \tag{2.6}$$

where w_α is the weighting factor. For the D2Q9 model, w_α is given by $w_0 = 4/9$, $w_{1-4} = 1/9$, and $w_{5-8} = 1/36$. The macroscopic density and momentum relate to the distribution functions and the discrete velocities via

$$\rho = \sum_\alpha f_\alpha, \text{ and } \rho\mathbf{u} = \sum_\alpha \mathbf{e}_\alpha f_\alpha + \frac{\delta t}{2}\mathbf{F}. \tag{2.7}$$

Rearranging Eq. (2.1), the streaming process can be expressed as

$$f_\alpha\left(\mathbf{x}+\mathbf{e}_\alpha\delta t, t+\delta t\right) = f_\alpha^*(\mathbf{x}, t), \tag{2.8}$$

where $f_\alpha^* = \mathbf{M}^{-1}\mathbf{m}^*$, and $\mathbf{m}^*$ is calculated algebraically given by

$$\mathbf{m}^* = \mathbf{m} - \mathbf{S}\left(\mathbf{m} - \mathbf{m}^{\mathrm{eq}}\right) + \delta t\left(\mathbf{I} - \frac{\mathbf{S}}{2}\right)\bar{\mathbf{F}}. \tag{2.9}$$

Here $\bar{\mathbf{F}}$ denotes the forcing term in the moment space (Yu and Fan, 2010):

$$\bar{\mathbf{F}} = \begin{bmatrix} 0 \\ 6(u_xF_x + u_yF_y) \\ -6(u_xF_x + u_yF_y) \\ F_x \\ -F_x \\ F_y \\ -F_y \\ 2(u_xF_x - u_yF_y) \\ (u_xF_y - u_yF_x) \end{bmatrix}. \tag{2.10}$$

2.2. Interparticle interactions

The interparticle interactions are accounted for using the pseudopotential model (Shan and Chen, 1993). For the single-component multiphase LBM, the force acting on a fluid node due to non-ideal interactions with its surroundings can be expressed as pair-wise interactions, given as (Shan and Chen, 1993; Shan, 2008)

$$\mathbf{F}_{\mathrm{ff}}(\boldsymbol{x}, t) = -G_{\mathrm{ff}}\psi(\boldsymbol{x}, t)\sum_\alpha w'_\alpha \psi\left(\boldsymbol{x} + \boldsymbol{e}_\alpha\delta t, t\right)\boldsymbol{e}_\alpha, \tag{2.11}$$

where G_{ff} is the fluid–fluid interaction strength, w'_α is the weighting factor with $w'_0 = 0$, $w'_{1-4} = 1/3$, and $w'_{5-8} = 1/12$, and $\psi(\boldsymbol{x}, t)$ is the pseudopotential. To be consistent with the EOS, the pseudopotential is taken as (Yuan and Schaefer, 2006)

$$\psi = \sqrt{\frac{2\left(p_{\mathrm{EOS}} - \rho c_s^2\right)}{G_{\mathrm{ff}}c^2}}. \tag{2.12}$$

Here the value of G_{ff} is determined such that the whole term inside the square root is positive, i.e., $G_{\mathrm{ff}} = -1$. p_{EOS} denotes a prescribed non-ideal EOS. Even though a non-ideal EOS is incorporated, simulation results of the liquid–vapor coexistence curves (phase diagram) may not follow the theoretical predictions obtained from the Maxwell equal-area construction, especially for the vapor branch (Kupershtokh et al., 2009; Chen et al., 2014). To alleviate the thermodynamic inconsistency caused by the use of the pseudopotential model, the improved force scheme is implemented given by (Li et al., 2013)

$$\bar{\mathbf{F}} = \begin{bmatrix} 0 \\ 6(u_xF_x + u_yF_y) + \frac{12\gamma|\mathbf{F}|^2}{\psi^2\delta t(\tau_e - 0.5)} \\ -6(u_xF_x + u_yF_y) - \frac{12\gamma|\mathbf{F}|^2}{\psi^2\delta t(\tau_\varepsilon - 0.5)} \\ F_x \\ -F_x \\ F_y \\ -F_y \\ 2(u_xF_x - u_yF_y) \\ (u_xF_y - u_yF_x) \end{bmatrix}, \tag{2.13}$$

where $|\mathbf{F}|^2 = \left(\mathrm{F}_x^2 + \mathrm{F}_y^2\right)$, and γ is a tuning parameter used to adjust the mechanical stability condition. Eq. (2.13), instead of Eq. (2.10), is employed to calculate the forcing term in Eq. (2.9).

For p_{EOS}, we consider a piecewise linear EOS (Colosqui et al., 2012)

$$p_{\mathrm{EOS}} = \begin{cases} \rho\theta_V, & \text{if } \rho \le \rho_1 \\ \rho_1\theta_V + \left(\rho - \rho_1\right)\theta_M, & \text{if } \rho_1 < \rho \le \rho_2 \\ \rho_1\theta_V + \left(\rho_2 - \rho_1\right)\theta_M + \left(\rho - \rho_2\right)\theta_L, & \text{if } \rho > \rho_2 \end{cases} \tag{2.14}$$

where θ_V, θ_L, and θ_M denote the slope of $p(\rho)$, i.e., $\partial p/\partial\rho$, in vapor-phase region, liquid-phase region, and the unstable branch ($\partial p/\partial\rho < 0$), respectively. The two unknowns ρ_1 and ρ_2, which specify the spinodal points, are obtained by solving a system of two equations (Colosqui et al., 2012) that describe (a) the mechanical equilibrium

$$\int_{\rho_V}^{\rho_L} \mathrm{d}p = \left(\rho_1 - \rho_V\right)\theta_V + \left(\rho_2 - \rho_1\right)\theta_M + \left(\rho_L - \rho_2\right)\theta_L = 0, \tag{2.15}$$

and (b) the chemical equilibrium

$$\int_{\rho_V}^{\rho_L} \frac{1}{\rho}\mathrm{d}p = \log\left(\frac{\rho_1}{\rho_V}\right)\theta_V + \log\left(\frac{\rho_2}{\rho_1}\right)\theta_M + \log\left(\frac{\rho_L}{\rho_2}\right)\theta_L = 0. \tag{2.16}$$

Compared to the classical EOS, this piecewise linear EOS provides the flexibility to adjust $\partial p/\partial\rho$ in different regions, and by setting appropriate values the resulting LBM model gives a better stability. In this work these parameters are set to be $\theta_V = 0.64c_s^2$, $\theta_L = c_s^2$, and $\theta_M = -0.08c_s^2$ (Li and Luo, 2014). Moreover, the desired density, as well as the density ratio between liquid and vapor phases, can be set directly without the need to run additional simulations (e.g., stationary droplet test) (Yuan and Schaefer, 2006).

2.3. Fluid-solid interactions

To be consistent with the interactions between fluid particles, the fluid-solid interaction is formulated in a similar manner as follows:

$$\mathbf{F}_{\mathrm{fw}}(\boldsymbol{x}, t) = -G_{\mathrm{fw}}\psi(\boldsymbol{x}, t)\sum_\alpha w'_\alpha S\left(\boldsymbol{x} + \boldsymbol{e}_\alpha\delta t, t\right)\boldsymbol{e}_\alpha, \tag{2.17}$$

where G_{fw} is a free parameter to tune the adsorptive strength of fluid to the solid ($G_{\mathrm{fw}} = -1$), and $S\left(\boldsymbol{x} + \boldsymbol{e}_\alpha\delta t, t\right)$ is the switch function given by

$$S\left(\boldsymbol{x} + \boldsymbol{e}_\alpha\delta t, t\right) = \phi(\boldsymbol{x}, t)\, s\left(\boldsymbol{x} + \boldsymbol{e}_\alpha\delta t, t\right). \tag{2.18}$$

Note that apart from the conventional switch function $s\left(\boldsymbol{x} + \boldsymbol{e}_\alpha\delta t, t\right)$, which is equal to 1 for a solid and 0 if otherwise, an additional term, $\phi(\boldsymbol{x}, t)$, is introduced to be an analog of $\psi\left(\boldsymbol{x} + \boldsymbol{e}_\alpha\delta t, t\right)$ in Eq. (2.11), i.e., we take $\phi(\boldsymbol{x}, t) = \psi(\boldsymbol{x}, t)$. With this choice, $S\left(\boldsymbol{x} + \boldsymbol{e}_\alpha\delta t, t\right)$ is comparable in magnitude to $\psi\left(\boldsymbol{x} + \boldsymbol{e}_\alpha\delta t, t\right)$ when $s\left(\boldsymbol{x} + \boldsymbol{e}_\alpha\delta t, t\right) = 1$ (Sukop and Thorne, 2006).

Following Li et al. (2019), an improved virtual-density scheme is used to calculate the density for the solid phase. This approach is considered superior as it retains relatively simple implementation for complex geometries, and overcomes unphysical mass transfer near the solid boundary that are commonly observed when using the virtual-density scheme (Leclaire et al., 2016; Akai et al., 2018). The formula is given by

$$\rho_w(\boldsymbol{x}) = \begin{cases} \kappa\hat{\rho}(\boldsymbol{x}), & \kappa \ge 1, \text{ for decreasing } \theta, \\ \hat{\rho}(\boldsymbol{x}) - \Delta\rho, & \Delta\rho \ge 0, \text{ for increasing } \theta, \end{cases} \tag{2.19}$$

where κ and $\Delta\rho$ are constants (note that $\Delta\rho$ is not the density difference between the two phases) which can be tuned to achieve different contact angles, and $\hat{\rho}(\boldsymbol{x})$ is given by

$$\hat{\rho}(\boldsymbol{x}) = \frac{\sum_\alpha w'_\alpha \rho\left(\boldsymbol{x} + \boldsymbol{e}_\alpha\delta t\right)\left(1 - s\left(\boldsymbol{x} + \boldsymbol{e}_\alpha\delta t\right)\right)}{\sum_\alpha w'_\alpha\left(1 - s\left(\boldsymbol{x} + \boldsymbol{e}_\alpha\delta t\right)\right)}. \tag{2.20}$$

No-slip boundary condition is imposed at the solid wall by applying the bounce-back scheme (Succi, 2001; Nie et al., 2002): fluid particle colliding with a wall is reversed and streamed in the opposite direction.

Table 1
Physical properties of liquid and vapor phases used in numerical simulations.

Parameter	Value	
	physical unit	lattice unit
Liquid density, ρ_L	994.5 kg/m^3	130.0
Vapor density, ρ_V	7.2 kg/m^3	0.9
Liquid kinematic viscosity, ν_L	0.6×10^{-6} m^2/s	0.25
Vapor kinematic viscosity, ν_V	1.3×10^{-6} m^2/s	0.5

Table 2
Coexistence densities and pressure difference between liquid and vapor phases at different radii (in lattice units).

r_0	ρ_L	ρ_V	$\Delta p\ (p_V - p_L)$
15	129.20	0.85	0.18
20	129.47	0.86	0.14
25	129.60	0.89	0.11
30	129.70	0.90	0.09
35	129.70	0.90	0.08

3. Validation

To verify the developed LBM model, two numerical tests are conducted, i.e., Laplace law and capillary intrusion. Physical properties of fluid phases are set to be representative for UHS in saline aquifers, with pressure and temperature given by 10 MPa and 45 °C, respectively (Yekta et al., 2018; Hashemi et al., 2021a). The resulting density and kinematic viscosity ratios for brine and H_2, i.e., ρ_L/ρ_V and ν_L/ν_V, are approximately 140 and 0.5. Table 1 lists physical parameters which are mutually used in the following simulations unless otherwise specified. "Liquid" and "Vapor" refer to brine and H_2, respectively. Note that the values are given in both physical and lattice units.

3.1. Laplace law

We start with the static test of Laplace law, which states that the pressure difference across the interface of a droplet is proportional to the inverse of the radius of the droplet, namely,

$$\Delta p = \frac{\sigma}{r}, \tag{3.1}$$

where σ is the surface tension. Simulations are performed in a square domain of 101×101 lattices. In each run, a bubble at a given radius r_0 is placed in the center surrounded by the liquid phase. The domain is fully periodic (in both x and y directions) and no external force is applied. Initial distribution of fluid density is given by (Huang et al., 2011)

$$\rho(x, y) = \frac{\rho_L + \rho_V}{2} + \frac{\rho_L - \rho_V}{2} \tanh\left[\frac{2(r - r_0)}{W}\right], \tag{3.2}$$

where $W = 5$, and $r = \sqrt{(x - x_0)^2 + (y - y_0)^2}$ with (x_0, y_0) being the centroid of the domain.

Five simulation runs are conducted with the initial radius of 15, 20, 25, 30, and 35 lattices. The parameter in Eq. (2.13), i.e., γ, is tuned to be 0.072 to meet the thermodynamic consistency. Density of both phases are recorded after reaching the steady state — see Table 2. As shown, ρ_L and ρ_V remain nearly constant at different radii, and are equal to the initial values shown in Table 1. This ensures the desired density contrast holds even if the interface exhibits varying curvatures in complex pore space. Pressure differences are further computed based on the density map, which are plotted as a function of the inverse of the radius shown in Fig. 1. It is observed that Δp is proportional to $1/r$, and the results fit well with the linear relation (dashed line) as expected by the Laplace law from Eq. (3.1). The slope indicates that the surface tension is 2.75.

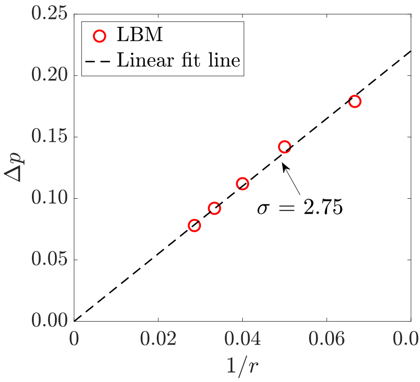

Fig. 1. Validation of Laplace law. Circles denote results obtained from LBM simulation, and the linear fit is depicted as a dashed line.

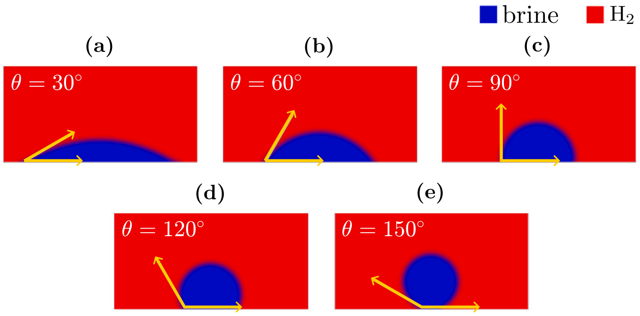

Fig. 2. Density distributions at steady-state with varying wettabilities.

Table 3
Values of tuning parameters for different contact angles.

$\theta/°$	κ	$\Delta\rho$
30	1.88	0
60	1.50	0
90	1.05	0
120	1.05	5.0
150	1.05	13.0

3.2. Capillary intrusion

Experimental observations have shown that the H_2-brine-rock system is in general water wet, i.e., the contact angle between the wetting (liquid) phase and the solid wall, θ, is smaller than 90°. To set a proper contact angle for the capillary intrusion test that involves fluid-solid interactions, we first establish the correlation between the wettability and tuning parameters (κ and $\Delta\rho$ in Eq. (2.19)). The density distribution of liquid and vapor phases on a flat solid surface is examined. The domain consists of 101×51 lattices with the bottom and top boundaries being solid walls, and the left and right boundaries being periodic. Simulation is initiated by placing a semi-circular liquid droplet with a radius of 20 on the bottom surface. Fig. 2 shows the density configurations at steady state. Different contact angles are achieved by tuning κ and $\Delta\rho$; their values of each case are listed in Table 3. As shown, a smaller contact angle is achieved by increasing κ, and a larger contact angle can be obtained by increasing $\Delta\rho$ meanwhile keeping κ to be equal to 1.05. For neutral wettability, $\kappa = 1.05$ ($\Delta\rho = 0$).

The capillary intrusion test is performed in a 2D capillary tube that has a hydrophilic inner surface. As shown in Fig. 3, the wetting liquid penetrates the tube that initially contains the non-wetting vapor phase. Movement of the interface is governed by the balance between capillary and viscous forces, which can be expressed as (Pooley et al., 2009; Liu

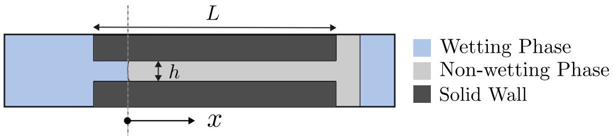

Fig. 3. Schematic of capillary intrusion test.

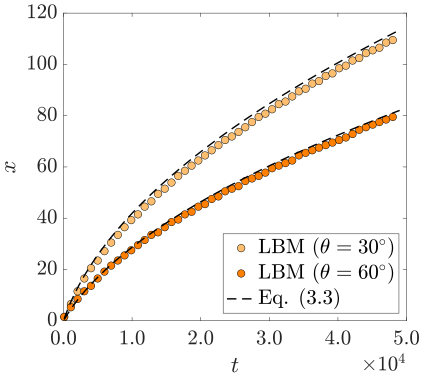

Fig. 4. Interface advancement in capillary intrusion test: comparisons between LBM results and theoretical predictions.

et al., 2014)

$$\sigma \cos(\theta) = \frac{6}{h}\left[\mu_L x + \mu_V (L - x)\right]\frac{\mathrm{d}x}{\mathrm{d}t}, \tag{3.3}$$

where L and h are the length and width of the capillary tube, respectively; $x(t)$ is the position of the interface as a function of time, μ_L and μ_V are dynamic viscosities of liquid and vapor phases. The domain is discretized into 400 × 35 lattice points with $L = 200$ and $h = 15$ for the capillary tube. Periodic boundary conditions are imposed on the region occupied by fluid.

We consider two scenarios with the contact angle given by $\theta = 30°$ and $60°$, both of which are water wet conditions. Origin of x-axis is set such that $x = 0$ at $t = 0$. Fig. 4 presents comparisons of interface advancement predicted from LBM simulations and the numerical solution of Eq. (3.3). It is observed that for the investigated cases, results obtained from the developed LBM model agree well with the theoretical predictions.

4. Simulation setup and pore-scale characterization

We investigate the H_2-brine system in a 2D porous medium with complex geometries. The porous medium is constructed by placing grains of varying radii on a square. These grains represent solid phase, and the remaining area are pore phase. The discrete domain consists of 601 × 601 lattice nodes, which are considered sufficiently large to derive meaningful constitutive relations (Li et al., 2018; Zhao et al., 2018; Nemer et al., 2020; Ji et al., 2022). As shown in Fig. 5a, nodes in gray and light blue denote solid and pore phases, respectively. The pore size of each node in the pore phase is calculated based on the medial axis of the porous medium (Zhao et al., 2016; Wang and Aryana, 2020), and the resulting distribution is presented in Fig. 5b. In this case, the pore size distribution has a mean value of 21.1 *lu*.

Fluid flow is driven by a constant body force in x direction, and a periodic boundary condition is imposed by adding five extra columns of pore nodes to both the inlet and outlet. No flow boundary condition is applied at the top and bottom boundaries. Fluids of different phases are initialized using the approach proposed by Li et al. (2018). We conduct simulations at two capillary numbers (Ca) by varying the body force F. Note that the standard definition of Ca is expressed as $\mathrm{Ca} = \mu v/\sigma$, where v is the characteristic velocity which is often determined by the injection rate. As the fluid is driven by the body force, here a modified Ca is used, which is given by $\mathrm{Ca} = \mathrm{F}/\sigma$ (Yiotis et al., 2007). Two contact angles are considered to account for different wettability conditions. The investigated capillary number ($\mathrm{Ca} = 3.6 \times 10^{-5}$ and 1.5×10^{-4}) and contact angle ($\theta = 30°$ and $60°$) fall within the reasonable range encountered in the UHS (Hashemi et al., 2021b; Higgs et al., 2022; Lysyy et al., 2023).

Flow simulation is performed for each case to examine the relative permeability of the H_2-brine system. The flux of each phase is calculated based on the velocity distribution in the entire domain given by (Zhao et al., 2018)

$$Q_\alpha = \frac{\sum u_{x\alpha}\delta x \delta y}{L_x}, \tag{4.1}$$

where δx and δy are the size of a lattice cell, L_x is the length of the medium, $u_{x\alpha}$ and Q_α are the local velocity and the total flux of phase α in x direction, respectively. The relative permeability ($k_{r\alpha}$) at a given saturation (S_α) is then calculated via:

$$k_{r\alpha}\left(S_\alpha\right) = \frac{Q_\alpha\left(S_\alpha\right)}{Q_\alpha\left(S_\alpha = 1\right)}. \tag{4.2}$$

Strictly speaking, Q_α is calculated after the system reaches the steady-state. However, given that the snap-off and bubble coalescence events persistently occur in this unstable system, determining the precise moment of reaching a steady state is a challenging task. Therefore, the mean value of Q_α, computed within a relatively narrow range of fluctuations at the late stage, is adopted in Eq. (4.2).

To better understand the fluid configuration from a pore-scale perspective, the Euler number and the interfacial area between the two phases are computed based on the fluid distribution at steady state. The Euler number is used to characterize the connectivity of one fluid phase (Herring et al., 2013; Rücker et al., 2015; Schlüter et al., 2016; Zhang et al., 2022) . For the 2D system, it is given by

$$\chi_\alpha = \beta_0 - \beta_1, \tag{4.3}$$

where β_0 is the number of discrete elements of phase α, and β_1 is the number of redundant loops presented in the fluid phase. Consider the porous medium (shown in Fig. 5a) is fully saturated with a single fluid phase α. In this case, $\beta_0 = 1$ and β_1 is equal to the total number of grains within the inner region of the domain, i.e., $\beta_1 = 121$, and the resulting $\chi_\alpha = 1 - 121 = -120$. Following (Herring et al., 2013), the normalized Euler number, $\hat{\chi}_\alpha$, defined as the ratio between the Euler number of a given fluid distribution and the Euler number at the fully saturated scenario ($\chi_\alpha = -120$), is used in the following discussions. This definition indicates that $\hat{\chi}_\alpha$ approaches 1.0 as the targeting phase reaches its maximum connectivity. Conversely, a more negative value suggests the presence of a larger number of disconnected clusters.

The fluid–fluid interfacial area, A_{wn}, is calculated using the following equation (Porter et al., 2010):

$$A_{wn} = \frac{1}{2}\left(A_w + A_n - A_s\right), \tag{4.4}$$

where A_w, A_n, and A_s denote the interfacial area for the wetting, non-wetting, and solid phases, respectively. They are evaluated by generating contours between phases, based on a single value chosen to separate one phase from the other ones.

5. Results and discussions

5.1. Fluid distribution at different saturations

The steady-state fluid distribution at three saturations ($S_w = 0.2$, 0.5, and 0.8) is presented in Fig. 6. At small S_w ($S_w = 0.2$), the wetting phase (brine) spreads along the surface of solid grains with differing behaviors. In Fig. 6(a), the liquid tends to fill pores and throats in both x and y directions. As Ca increases, the liquid film becomes thinner and it coats a larger number of solid grains, leading to a

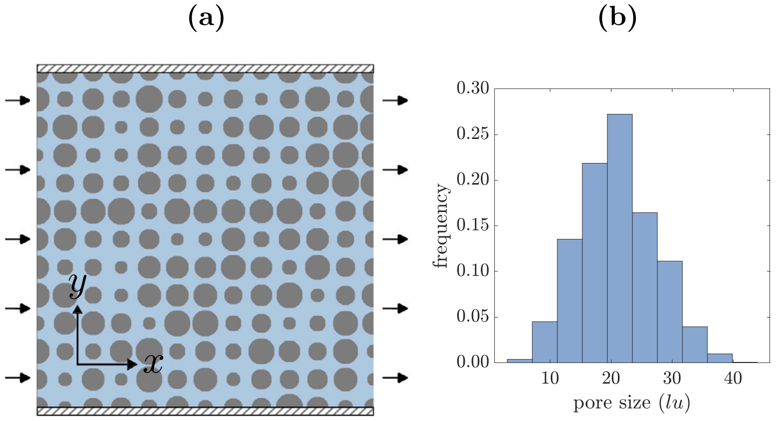

Fig. 5. The synthetic porous medium used in flow simulation. (a) pore geometry and (b) pore size distribution.

more tortuous configuration of interconnected coated grains (Fig. 6(d)). This results in an improved fluid connectivity for the liquid phase ($\hat{\chi}_w$), along with an increase in interfacial area (A_{wn}) (Figs. 8(a) and 8(b)). Simultaneously, $\hat{\chi}_n$ decreases because the snap-off becomes more frequent (Tsai and Miksis, 1994; Roman et al., 2017). When θ increases from 30° to 60°, the number of liquid films, which bridge the solid grains in the direction perpendicular to the main flow, is reduced due to the weakened affinity of the medium to the wetting phase (Fig. 6(g)). As a result, the liquid phase prefers to coat the solid grains along the x direction. We also observe that the surfaces of some solid grains are partially covered by the liquid, rather than being fully immersed in the wetting phase.

For intermediate S_w ($S_w = 0.5$), the gas occupies the flow paths with wide pore throats, while the liquid flows through the narrower ones. Note that regardless of varying flow conditions, fluid distributions exhibit a similar pattern: the vapor phase forms large clusters in the upper half of the domain characterized by a relatively large and uniform pore size, whereas in the lower half of the domain, vapor phase tends to disperse into disconnected ganglia due to a more divergent pore size distribution (Figs. 6(b), 6(e), 6(h)). This observation is also quantitatively evident in the connectivity measurement of both phases, i.e., $\hat{\chi}_w$ and $\hat{\chi}_n$ at $S_w = 0.4$ and 0.6 shown in Fig. 8(a). Eventually at large S_w ($S_w = 0.8$), the vapor phase remains in the large pore space, gathered in the upper half of the domain (Figs. 6(d), (h), and (l)).

5.2. *Relative permeability: pore-scale analysis*

The total flux of each phase is recorded to determine if the system reaches steady-state. For example, Fig. 7 shows the temporal evolution of total fluxes in the case of Ca = 3.6×10^{-5} and $\theta = 30°$. In each plot, the dashed line indicates the Q_α that will be used to compute relative permeability. The resulting curves are shown in Fig. 8(c). We observe that at a given S_w, the wetting phase curves demonstrate slight variations compared to those of the nonwetting phase. k_{rw} increases monotonically along with S_w. It is worth mentioning that a larger θ leads to a higher k_{rw}, especially within the range of small to intermediate values of S_w. Mechanistically speaking, a stronger wettability enhances the interactions between the wetting phase and the solid surface. On one hand, a stronger adsorptive force hinders fluid detachment from the surface, thereby impeding the flow. On the other hand, it promotes the connectivity of wetting phase (Li et al., 2005). At the same Ca (Ca = 1.5×10^{-4}), a smaller θ gives a better connectivity (Fig. 8(a)). Nevertheless, k_{rw} is higher at $\theta = 60°$. This indicates the former mechanism dominants in the investigated case. One may expect the relative permeability of both phases increase with Ca, as demonstrated in previous work where both fluids are assumed to have equal density and viscosity (Li et al., 2005; Zhao et al., 2017). However, this is not what we observe as Ca increases from 3.6×10^{-5} to 1.5×10^{-4} with $\theta = 30°$. Instead, k_{rn} decreases at a higher Ca. In the simulated UHS system, there is a notable contrast in physical properties between H_2 and brine. Due to its considerably lower dynamic viscosity, the non-wetting phase demonstrates higher mobility which facilitates the fluid–fluid interactions between the phases at a higher Ca, as shown in Fig. 8(b), leading to a more curved (and reduced) k_{rn} (Bachu and Bennion, 2008).

As mentioned earlier, the relative permeability of wetting phase increases along with the phase saturation in a nearly quadratic manner; in contrast, the relative permeability of non-wetting phase exhibits pronounced variations under different settings. To further quantify the strength of correlation between relative permeability and saturation, as well as the pore-scale parameters, the Pearson correlation coefficient, $\rho(X, Y)$ (X and Y are random variables) (Cohen et al., 2009) is computed and the results are presented in Fig. 9. The values range from −1 to 1 with 1 indicating a perfect linear positive relation, and vice versa for -1. A small absolute value implies a weak linear dependency between the variables.

In the case of wetting phase, we observe a strong correlation between the relative permeability and phase saturation, i.e., $\rho(k_{rw}, S_w) = 0.99$. Besides, there is an observable dependency between k_{rw} and the Euler number of the wetting phase, as well as the interfacial area of two fluids: $\rho(k_{rw}, \hat{\chi}_w) = 0.74$, and $\rho(k_{rw}, A_{wn}) = -0.79$. Nevertheless, $\hat{\chi}_w$ and A_{wn} are fairly correlated with S_w. This suggests that k_{rw} can be described based on S_w solely. In the non-wetting case, S_n, $\hat{\chi}_n$, and A_{wn} are all positively correlated with k_{rn}: $\rho(k_{rn}, S_n) = 0.89$, $\rho(k_{rn}, \hat{\chi}_n) = 0.59$, and $\rho(k_{rn}, A_{wn}) = 0.52$. Similar to the wetting phase, k_{rn} shows a stronger dependency on the phase saturation compared to the pore-scale parameters, i.e., $\hat{\chi}_n$ and A_{wn}, which are also moderately correlated with S_n. However, k_{rn} exhibits more variations at large S_n (shown in Fig. 8(c)), indicating saturation alone is insufficient to characterize k_{rn}; $\hat{\chi}_n$, which acts more independently than A_{wn}, appears to be another state parameter that should be taken into account.

5.3. *Relative permeability: quantitative descriptions*

Motivated by the correlation matrix between relative permeability and state variables, we propose the following formulations for calculating the relative permeability:

$$K_{rw} = a_w S_w^2, \text{ and } K_{rn} = a_n S_n^{b_n + |\hat{\chi}_n|}. \tag{5.1}$$

Here a_w, a_n and b_n are fitting parameters and their values are optimized using the least squares method. Fig. 10 shows the comparison of relative permeability values calculated based on simulation results and those predicted by the proposed formulations. The coefficients of determination for the wetting and non-wetting phases are given by

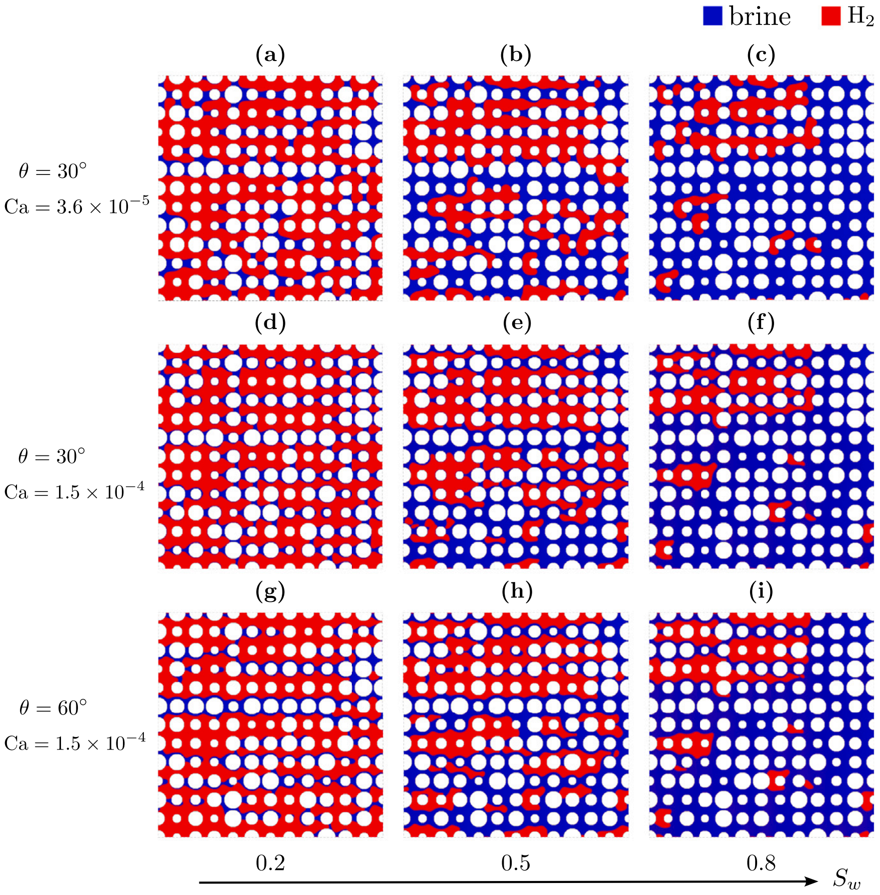

Fig. 6. Fluid distribution at steady-state for different capillary numbers and contact angles. The three maps in each column have identical wetting phase saturation.

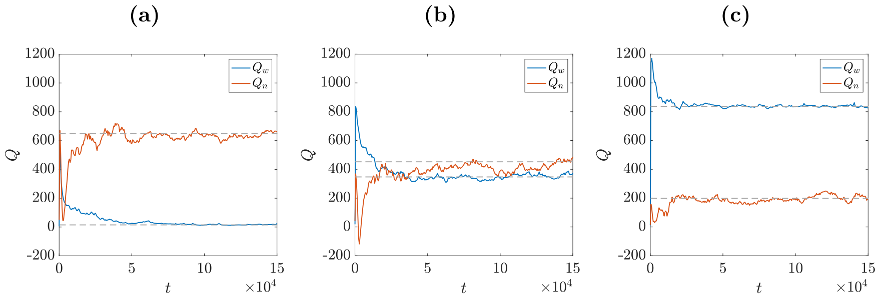

Fig. 7. The total flux of each phase in the case of $\mathrm{Ca} = 3.6 \times 10^{-5}$ and $\theta = 30^\circ$ at three saturation (S_w) values: (a) 0.2, (b) 0.5, and (c) 0.8.

0.989 and 0.974, respectively, indicating the proposed formulations offer favorable approximations of the data obtained from numerical simulations. Specifically, a good agreement between computed K_{rw} and $a_w S_w^2$ validates our hypothesis that K_{rw} is proportional to S_w^2. As for the non-wetting phase, we observe that the discrepancy increases at $S_n = 0.8$. This could potentially be attributed to a stronger interference between the two phases, which deserves a further investigation.

Our observations are consistent with the results from both experimental and numerical efforts reported in literature (Oak et al., 1990; Nguyen et al., 2006; Picchi and Battiato, 2019; Hashemi et al., 2021a): in a water-wet system, the gas and liquid phases demonstrate differing characteristics in their relative permeability curves. K_{rw} has a concave curve which is described using the quadratic form of S_w. However, K_{rn} tends to have a linear or convex shape. Note that recent experimental measurements show that the relative permeability curve for H_2 in the H_2-brine system also exhibits a concave shape (Lysyy et al., 2022; Higgs et al., 2024). The concave shape usually indicates the rock samples have a relatively uniform pore throat size (Wan et al., 2019). That is to say, the pore geometry plays a role in shaping the relative permeability curves, which highlights the need for a further exploration as well.

We design our numerical simulations to mimic steady-state experiments in which both fluids move simultaneously (Aryana and Kovscek, 2013; Berg et al., 2016). Therefore, the descriptions of relative permeability are established under steady-state conditions without specifying the process (drainage or imbibition). In UHS, however, H_2 is injected and reproduced cyclically, leading to a path-dependent behavior of constitutive relations, i.e., hysteresis (Juanes et al., 2006; Khorsandi et al., 2017; Wang et al., 2022; Boon and Hajibeygi, 2022; Lysyy et al., 2022). To properly capture hysteretic effect in LBM simulations, Ramstad et al. (2012) suggests to establish new phase saturations by injecting the fluid into the model according to the previously established steady-state fluid configuration. This ensures that the saturation changes in accordance with the desired path. Impacts of the flow path on the relative permeability for the UHS system will be investigated in the

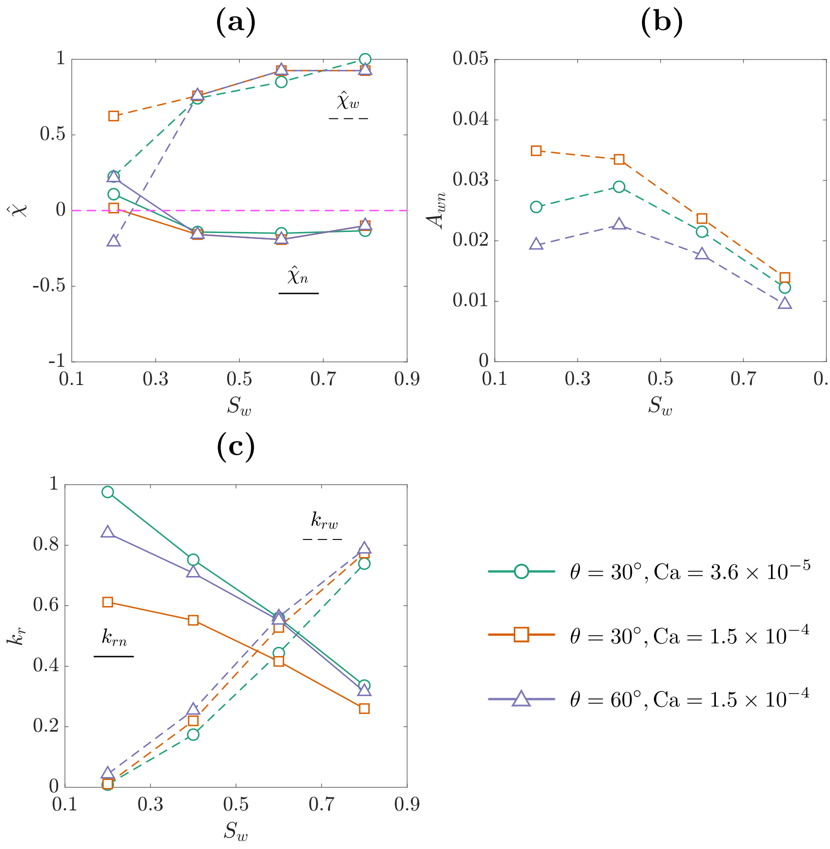

Fig. 8. Pore-scale parameters and relative permeability curves as functions of S_w.

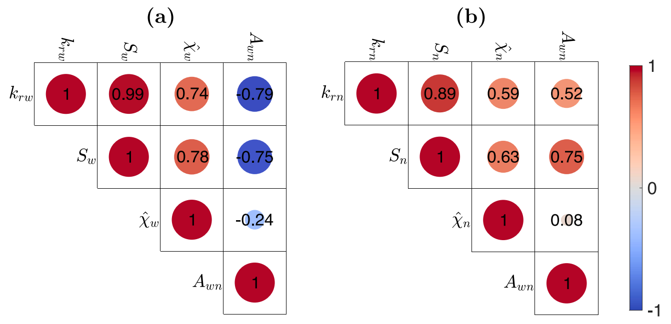

Fig. 9. Pearson correlation coefficients between relative permeability and state variables for the (a) wetting and (b) non-wetting phase.

next step. The gained insight from this work motivates us to derive simplified models based on the primary influential state parameters.

It should be noted that for the SCMP pseudopotential model, the two phases are treated as an immiscible pair: we focus on quantifying the two-phase flow interactions, i.e., relative permeability, between H_2 and brine. Therefore, the interphase mass transfer of H_2 in brine is not considered. Nevertheless, H_2 has a relatively high diffusivity that affects the pore-scale flow and transport processes, such as Ostwald Ripening (Mehmani and Xu, 2022; Zhang et al., 2023; Goodarzi et al., 2024). A possible direction for future development is to extend the current model to a multi-component and multiphase (MCMP) system. This affords the capability to incorporate diffusion/dissolution for more practical applications.

6. Conclusion

In this work, a physically-validated LBM model is developed to investigate the pore-scale dynamics of immiscible two-fluid system relevant for UHS. To capture the significant contrast of fluid properties commonly encountered in the UHS system, we utilize a single-component, two-phase pseudopotential model. This model incorporates an improved force scheme to ensure thermodynamic consistency. Furthermore, a piecewise linear EOS is used to provide local control of pressure derivatives with respect to the density, thereby achieving a superior stability. To verify the developed numerical model, we first conduct the static Laplace test, where the contrast of fluid properties are set to represent a typical UHS system. Results show that the pressure differences across the interface, obtained from varying radii of the liquid droplet, comply with the Laplace law. Next we examine the dynamic process of capillary intrusion under a wetting condition at two contact angles. The numerical model captures the movement of the interface predicted from theoretical solutions.

The developed model is then used to simulate the two phase flow of H_2-brine within a synthetic porous medium. Fluid distribution patterns at steady-state are characterized using the Euler number and the interfacial area between two fluids. A higher capillary number and a smaller contact angle promote the snap-off of the non-wetting phase, leading to reduced connectivity. The corresponding relative permeability of each phase is computed as a function of phase saturation. H_2 and brine demonstrate distinct behaviors in the investigated scenarios. In the case of brine, the relative permeability is adequately characterized by the quadratic expression of phase saturation. However, for H_2, its relative permeability depends on both phase saturation and the Euler number. Quantitative descriptions are finally established to evaluate the relative permeability given a fluid distribution. The developed model provides

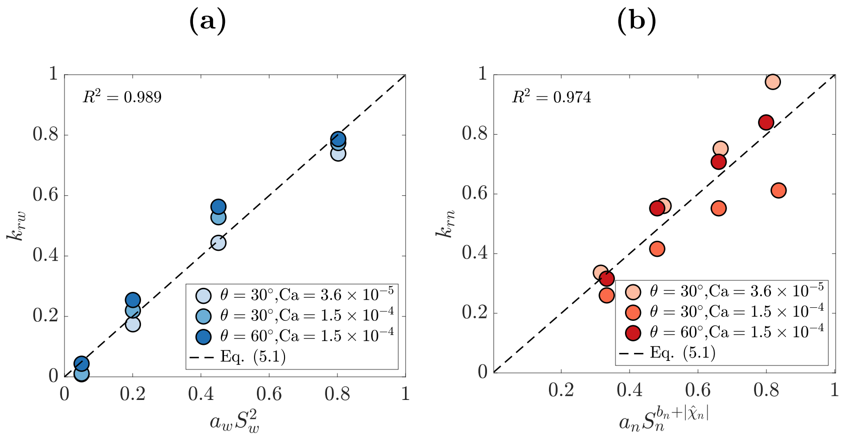

Fig. 10. Comparison of relative permeability values obtained from simulation results and the proposed formulations for the (a) wetting and (b) non-wetting phase.

an efficient alternative to laboratory experiments, enabling direct simulations of two-phase flow that involves a significant contrast of fluid properties.

CRediT authorship contribution statement

Yuhang Wang: Writing – original draft, Methodology, Funding acquisition, Formal analysis, Conceptualization, Software. **Thejas Hulikal Chakrapani:** Methodology, Formal analysis, Validation, Writing – original draft. **Zhang Wen:** Writing – review & editing, Supervision, Resources. **Hadi Hajibeygi:** Writing – review & editing, Supervision, Funding acquisition, Conceptualization, Methodology.

Declaration of competing interest

The authors declare that they have no known competing financial interests or personal relationships that could have appeared to influence the work reported in this paper.

Data availability

Data will be made available on request.

Acknowledgments

Yuhang Wang was supported by National Natural Science Foundation of China (No. 42307098) and the "CUG Scholar" Scientific Research Funds at China University of Geosciences (Wuhan) (Project No. 2022157). Hadi Hajibeygi was sponsored by the Dutch National Science Foundation (NWO) under Vidi Talent Program Project "ADMIRE" (Project No. 17509).

References

Akai, T., Bijeljic, B., Blunt, M.J., 2018. Wetting boundary condition for the color-gradient lattice Boltzmann method: Validation with analytical and experimental data. Adv. Water Resour. 116, 56–66.

Aryana, S.A., Kovscek, A.R., 2013. Nonequilibrium effects and multiphase flow in porous media. Transp. Porous Media 97, 373–394.

Bachu, S., Bennion, B., 2008. Effects of in-situ conditions on relative permeability characteristics of CO_2-brine systems. Environ. Geol. 54, 1707–1722.

Berg, S., Rücker, M., Ott, H., Georgiadis, A., Van der Linde, H., Enzmann, F., Kersten, M., Armstrong, R., De With, S., Becker, J., Wiegmann, A., 2016. Connected pathway relative permeability from pore-scale imaging of imbibition. Adv. Water Resour. 90, 24–35.

Blunt, M.J., 2017. Multiphase Flow in Permeable Media: A Pore-Scale Perspective. Cambridge University Press.

Bo, Z., Boon, M., Hajibeygi, H., Hurter, S., 2023. Impact of experimentally measured relative permeability hysteresis on reservoir-scale performance of underground hydrogen storage (UHS). Int. J. Hydrog. Energy 48 (36), 13527–13542.

Boon, M., Hajibeygi, H., 2022. Experimental characterization of H_2/water multiphase flow in heterogeneous sandstone rock at the core scale relevant for underground hydrogen storage (UHS). Sci. Rep. 12 (1), 14604.

Chai, M., Chen, Z., Nourozieh, H., Yang, M., 2023. Numerical simulation of large-scale seasonal hydrogen storage in an anticline aquifer: A case study capturing hydrogen interactions and cushion gas injection. Appl. Energy 334, 120655.

Chen, L., Kang, Q., Mu, Y., He, Y.-L., Tao, W.-Q., 2014. A critical review of the pseudopotential multiphase lattice Boltzmann model: Methods and applications. Int. J. Heat Mass Transfer 76, 210–236.

Cohen, I., Huang, Y., Chen, J., Benesty, J., Benesty, J., Chen, J., Huang, Y., Cohen, I., 2009. Pearson correlation coefficient. Noise Reduct. Speech Process. 1–4.

Colosqui, C.E., Falcucci, G., Ubertini, S., Succi, S., 2012. Mesoscopic simulation of non-ideal fluids with self-tuning of the equation of state. Soft Matter 8 (14), 3798–3809.

d'Humières, D., 2002. Multiple–relaxation–time lattice Boltzmann models in three dimensions. Philos. Trans. R. Soc. Lond. Ser. A Math. Phys. Eng. Sci. 360 (1792), 437–451.

Eller, J., Sauerborn, T., Becker, B., Buntic, I., Gross, J., Helmig, R., 2022. Modeling subsurface hydrogen storage with transport properties from entropy scaling using the PC-SAFT equation of state. Water Resour. Res. 58 (4), e2021WR030885.

Gahleitner, G., 2013. Hydrogen from renewable electricity: An international review of power-to-gas pilot plants for stationary applications. Int. J. Hydrog. Energy 38 (5), 2039–2061.

Gong, Y., Sedghi, M., Piri, M., 2021a. Dynamic pore-scale modeling of residual trapping following imbibition in a rough-walled fracture. Transp. Porous Media 140 (1), 143–179.

Gong, Y., Sedghi, M., Piri, M., 2021b. Two-phase relative permeability of rough-walled fractures: A dynamic pore-scale modeling of the effects of aperture geometry. Water Resour. Res. 57 (12), e2021WR030104.

Goodarzi, S., Zhang, Y., Foroughi, S., Bijeljic, B., Blunt, M.J., 2024. Trapping, hysteresis and Ostwald ripening in hydrogen storage: A pore-scale imaging study. Int. J. Hydrog. Energy 56, 1139–1151.

Gunstensen, A.K., Rothman, D.H., Zaleski, S., Zanetti, G., 1991. Lattice Boltzmann model of immiscible fluids. Phys. Rev. A 43 (8), 4320.

Hashemi, L., Blunt, M., Hajibeygi, H., 2021a. Pore-scale modelling and sensitivity analyses of hydrogen-brine multiphase flow in geological porous media. Sci. Rep. 11 (1), 1–13.

Hashemi, L., Glerum, W., Farajzadeh, R., Hajibeygi, H., 2021b. Contact angle measurement for hydrogen/brine/sandstone system using captive-bubble method relevant for underground hydrogen storage. Adv. Water Resour. 154, 103964.

He, X., Chen, S., Zhang, R., 1999. A lattice Boltzmann scheme for incompressible multiphase flow and its application in simulation of Rayleigh–Taylor instability. J. Comput. Phys. 152 (2), 642–663.

He, X., Luo, L.S., 1997. Theory of the lattice Boltzmann method: From the Boltzmann equation to the lattice Boltzmann equation. Phys. Rev. E 56 (6), 6811.

Heinemann, N., Alcalde, J., Miocic, J.M., Hangx, S.J., Kallmeyer, J., Ostertag-Henning, C., Hassanpouryouzband, A., Thaysen, E.M., Strobel, G.J., Schmidt-Hattenberger, C., Edlmann, K., Wilkinson, M., Bentham, M., Haszeldine, R.S., Carbonell, R., Rudloff, A., 2021. Enabling large-scale hydrogen storage in porous media–the scientific challenges. Energy Environ. Sci. 14 (2), 853–864.

Hematpur, H., Abdollahi, R., Rostami, S., Haghighi, M., Blunt, M.J., 2023. Review of underground hydrogen storage: Concepts and challenges. Adv. Geo-Energy Res. 7 (2), 111–131.

Herring, A.L., Harper, E.J., Andersson, L., Sheppard, A., Bay, B.K., Wildenschild, D., 2013. Effect of fluid topology on residual nonwetting phase trapping: Implications for geologic CO2 sequestration. Adv. Water Resour. 62, 47–58.

Higgs, S., Da Wang, Y., Sun, C., Ennis-King, J., Jackson, S.J., Armstrong, R.T., Mostaghimi, P., 2022. In-situ hydrogen wettability characterisation for underground hydrogen storage. Int. J. Hydrog. Energy 47 (26), 13062–13075.

Higgs, S., Da Wang, Y., Sun, C., Ennis-King, J., Jackson, S.J., Armstrong, R.T., Mostaghimi, P., 2024. Direct measurement of hydrogen relative permeability hysteresis for underground hydrogen storage. Int. J. Hydrog. Energy 50, 524–541.

Hosseini, M., Fahimpour, J., Ali, M., Keshavarz, A., Iglauer, S., 2022. H_2-brine interfacial tension as a function of salinity, temperature, and pressure; implications for hydrogen geo-storage. J. Pet. Sci. Eng. 213, 110441.

Huang, H., Krafczyk, M., Lu, X., 2011. Forcing term in single-phase and Shan-Chen-type multiphase lattice Boltzmann models. Phys. Rev. E 84 (4), 046710.

Huang, H., Li, Z., Liu, S., Lu, X.-Y., 2009. Shan-and-Chen-type multiphase lattice Boltzmann study of viscous coupling effects for two-phase flow in porous media. Internat. J. Numer. Methods Fluids 61 (3), 341–354.

Iglauer, S., Ali, M., Keshavarz, A., 2021. Hydrogen wettability of sandstone reservoirs: Implications for hydrogen geo-storage. Geophys. Res. Lett. 48 (3), e2020GL090814.

Jangda, Z., Menke, H., Busch, A., Geiger, S., Bultreys, T., Lewis, H., Singh, K., 2023. Pore-scale visualization of hydrogen storage in a sandstone at subsurface pressure and temperature conditions: Trapping, dissolution and wettability. J. Colloid Interface Sci. 629, 316–325.

Ji, Y., Kneafsey, T.J., Hou, J., Zhao, J., Liu, C., Guo, T., Wei, B., Zhao, E., Bai, Y., 2022. Relative permeability of gas and water flow in hydrate-bearing porous media: A micro-scale study by lattice Boltzmann simulation. Fuel 321, 124013.

Joekar-Niasar, V., Hassanizadeh, S., 2012. Analysis of fundamentals of two-phase flow in porous media using dynamic pore-network models: A review. Crit. Rev. Environ. Sci. Technol. 42 (18), 1895–1976.

Juanes, R., Spiteri, E., Orr Jr., F., Blunt, M., 2006. Impact of relative permeability hysteresis on geological CO2 storage. Water Resour. Res. 42 (12).

Khorsandi, S., Li, L., Johns, R.T., 2017. Equation of state for relative permeability, including hysteresis and wettability alteration. SPE J. 22 (06), 1915–1928.

Krevor, S., De Coninck, H., Gasda, S.E., Ghaleigh, N.S., de Gooyert, V., Hajibeygi, H., Juanes, R., Neufeld, J., Roberts, J.J., Swennenhuis, F., 2023. Subsurface carbon dioxide and hydrogen storage for a sustainable energy future. Nat. Rev. Earth Environ. 4 (2), 102–118.

Kupershtokh, A.L., Medvedev, D., Karpov, D., 2009. On equations of state in a lattice Boltzmann method. Comput. Math. Appl. 58 (5), 965–974.

Lallemand, P., Luo, L.S., 2000. Theory of the lattice Boltzmann method: dispersion, dissipation, isotropy, Galilean invariance, and stability. Phys. Rev. E 61 (6), 6546.

Leclaire, S., Abahri, K., Belarbi, R., Bennacer, R., 2016. Modeling of static contact angles with curved boundaries using a multiphase lattice Boltzmann method with variable density and viscosity ratios. Internat. J. Numer. Methods Fluids 82 (8), 451–470.

Li, Z., Galindo-Torres, S., Yan, G., Scheuermann, A., Li, L., 2018. A lattice Boltzmann investigation of steady-state fluid distribution, capillary pressure and relative permeability of a porous medium: Effects of fluid and geometrical properties. Adv. Water Resour. 116, 153–166.

Li, Q., Luo, K., 2014. Thermodynamic consistency of the pseudopotential lattice Boltzmann model for simulating liquid–vapor flows. Appl. Therm. Eng. 72 (1), 56–61.

Li, Q., Luo, K., Li, X., 2013. Lattice Boltzmann modeling of multiphase flows at large density ratio with an improved pseudopotential model. Phys. Rev. E 87 (5), 053301.

Li, H., Pan, C., Miller, C.T., 2005. Pore-scale investigation of viscous coupling effects for two-phase flow in porous media. Phys. Rev. E 72 (2), 026705.

Li, Q., Yu, Y., Luo, K.H., 2019. Implementation of contact angles in pseudopotential lattice Boltzmann simulations with curved boundaries. Phys. Rev. E 100 (5), 053313.

Liu, H., Kang, Q., Leonardi, C.R., Schmieschek, S., Narváez, A., Jones, B.D., Williams, J.R., Valocchi, A.J., Harting, J., 2016. Multiphase lattice Boltzmann simulations for porous media applications: A review. Comput. Geosci. 20, 777–805.

Liu, H., Valocchi, A.J., Werth, C., Kang, Q., Oostrom, M., 2014. Pore-scale simulation of liquid CO2 displacement of water using a two-phase lattice Boltzmann model. Adv. Water Resour. 73, 144–158.

Liu, L., Wang, Y., Aryana, S.A., 2021. Insights into scale translation of methane transport in nanopores. J. Nat. Gas Sci. Eng. 96, 104220.

Lord, A.S., Kobos, P.H., Borns, D.J., 2014. Geologic storage of hydrogen: Scaling up to meet city transportation demands. Int. J. Hydrog. Energy 39 (28), 15570–15582.

Luboń, K., Tarkowski, R., 2020. Numerical simulation of hydrogen injection and withdrawal to and from a deep aquifer in NW Poland. Int. J. Hydrog. Energy 45 (3), 2068–2083.

Lysyy, M., Føyen, T., Johannesen, E.B., Fernø, M., Ersland, G., 2022. Hydrogen relative permeability hysteresis in underground storage. Geophys. Res. Lett. 49 (17), e2022GL100364.

Lysyy, M., Liu, N., Solstad, C.M., Fernø, M.A., Ersland, G., 2023. Microfluidic hydrogen storage capacity and residual trapping during cyclic injections: Implications for underground storage. Int. J. Hydrog. Energy.

Meakin, P., Tartakovsky, A.M., 2009. Modeling and simulation of pore-scale multiphase fluid flow and reactive transport in fractured and porous media. Rev. Geophys. 47 (3).

Mehmani, Y., Xu, K., 2022. Pore-network modeling of Ostwald ripening in porous media: How do trapped bubbles equilibrate? J. Comput. Phys. 457, 111041.

Mukherjee, S., Abraham, J., 2007. A pressure-evolution-based multi-relaxation-time high-density-ratio two-phase lattice-Boltzmann model. Comput. & Fluids 36 (6), 1149–1158.

Nemer, M.N., Rao, P.R., Schaefer, L., 2020. Wettability alteration implications on pore-scale multiphase flow in porous media using the lattice Boltzmann method. Adv. Water Resour. 146, 103790.

Nguyen, V.H., Sheppard, A.P., Knackstedt, M.A., Pinczewski, W.V., 2006. The effect of displacement rate on imbibition relative permeability and residual saturation. J. Pet. Sci. Eng. 52 (1–4), 54–70.

Nie, X., Doolen, G.D., Chen, S., 2002. Lattice-Boltzmann simulations of fluid flows in MEMS. J. Stat. Phys. 107 (1), 279–289.

Oak, M.J., Baker, L.E., Thomas, D., 1990. Three-phase relative permeability of Berea sandstone. J. Pet. Technol. 42 (08), 1054–1061.

Pan, B., Liu, K., Ren, B., Zhang, M., Ju, Y., Gu, J., Zhang, X., Clarkson, C.R., Edlmann, K., Zhu, W., Iglauer, S., 2023. Impacts of relative permeability hysteresis, wettability, and injection/withdrawal schemes on underground hydrogen storage in saline aquifers. Fuel 333, 126516.

Pfeiffer, W.T., Bauer, S., 2015. Subsurface porous media hydrogen storage–scenario development and simulation. Energy Procedia 76, 565–572.

Picchi, D., Battiato, I., 2019. Relative permeability scaling from pore-scale flow regimes. Water Resour. Res. 55 (4), 3215–3233.

Piri, M., Blunt, M.J., 2005. Three-dimensional mixed-wet random pore-scale network modeling of two-and three-phase flow in porous media. I. Model description. Phys. Rev. E 71 (2), 026301.

Pooley, C., Kusumaatmaja, H., Yeomans, J., 2009. Modelling capillary filling dynamics using lattice Boltzmann simulations. Eur. Phys. J. Spec. Top. 171, 63–71.

Porter, M.L., Wildenschild, D., Grant, G., Gerhard, J.I., 2010. Measurement and prediction of the relationship between capillary pressure, saturation, and interfacial area in a NAPL-water-glass bead system. Water Resour. Res. 46 (8).

Prodanović, M., Bryant, S.L., 2006. A level set method for determining critical curvatures for drainage and imbibition. J. Colloid Interface Sci. 304 (2), 442–458.

Qin, F., Zhao, J., Kang, Q., Derome, D., Carmeliet, J., 2021. Lattice Boltzmann modeling of drying of porous media considering contact angle hysteresis. Transp. Porous Media 140, 395–420.

Raeini, A.Q., Blunt, M.J., Bijeljic, B., 2012. Modelling two-phase flow in porous media at the pore scale using the volume-of-fluid method. J. Comput. Phys. 231 (17), 5653–5668.

Ramstad, T., Idowu, N., Nardi, C., Øren, P.E., 2012. Relative permeability calculations from two-phase flow simulations directly on digital images of porous rocks. Transp. Porous Media 94 (2), 487–504.

Roman, S., Abu-Al-Saud, M.O., Tokunaga, T., Wan, J., Kovscek, A.R., Tchelepi, H.A., 2017. Measurements and simulation of liquid films during drainage displacements and snap-off in constricted capillary tubes. J. Colloid Interface Sci. 507, 279–289.

Rücker, M., Berg, S., Armstrong, R., Georgiadis, A., Ott, H., Schwing, A., Neiteler, R., Brussee, N., Makurat, A., Leu, L., Wolf, M., Khan, F., Enzmann, F., Kersten, M., 2015. From connected pathway flow to ganglion dynamics. Geophys. Res. Lett. 42 (10), 3888–3894.

Schlüter, S., Berg, S., Rücker, M., Armstrong, R., Vogel, H.J., Hilfer, R., Wildenschild, D., 2016. Pore-scale displacement mechanisms as a source of hysteresis for two-phase flow in porous media. Water Resour. Res. 52 (3), 2194–2205.

Shan, X., 2008. Pressure tensor calculation in a class of nonideal gas lattice Boltzmann models. Phys. Rev. E 77 (6), 066702.

Shan, X., Chen, H., 1993. Lattice Boltzmann model for simulating flows with multiple phases and components. Phys. Rev. E 47 (3), 1815.

Son, S., Chen, L., Kang, Q., Derome, D., Carmeliet, J., 2016. Contact angle effects on pore and corner arc menisci in polygonal capillary tubes studied with the pseudopotential multiphase lattice Boltzmann model. Computation 4 (1), 12.

Succi, S., 2001. The Lattice Boltzmann Equation: For Fluid Dynamics and Beyond. Oxford University Press.

Sukop, M.C., Thorne, D.T., 2006. Lattice Boltzmann Modeling: An Introduction for Geoscientists and Engineers. Springer Berlin, Heidelberg.

Swift, M.R., Osborn, W., Yeomans, J., 1995. Lattice Boltzmann simulation of nonideal fluids. Phys. Rev. Lett. 75 (5), 830.

Tarkowski, R., 2019. Underground hydrogen storage: Characteristics and prospects. Renew. Sustain. Energy Rev. 105, 86–94.

Tsai, T., Miksis, M.J., 1994. Dynamics of a drop in a constricted capillary tube. J. Fluid Mech. 274, 197–217.

Valvatne, P.H., Blunt, M.J., 2004. Predictive pore-scale modeling of two-phase flow in mixed wet media. Water Resour. Res. 40 (7).

van Rooijen, W., Hashemi, L., Boon, M., Farajzadeh, R., Hajibeygi, H., 2022. Microfluidics-based analysis of dynamic contact angles relevant for underground hydrogen storage. Adv. Water Resour. 164, 104221.

Wan, T., Yang, S., Wang, L., Sun, L., 2019. Experimental investigation of two-phase relative permeability of gas and water for tight gas carbonate under different test conditions. Oil Gas Sci. Technol.–Revue d'IFP Energ. nouvelles 74, 23.

Wang, Y., Aryana, S.A., 2020. Pore-scale simulation of gas flow in microscopic permeable media with complex geometries. J. Nat. Gas Sci. Eng. 81, 103441.

Wang, Y., Vuik, C., Hajibeygi, H., 2022. Analysis of hydrodynamic trapping interactions during full-cycle injection and migration of CO2 in deep saline aquifers. Adv. Water Resour. 159, 104073.

Wang, J., Yang, Y., Cai, S., Yao, J., Xie, Q., 2023. Pore-scale modelling on hydrogen transport in porous media: Implications for hydrogen storage in saline aquifers. Int. J. Hydrog. Energy 48 (37), 13922–13933.

Yekta, A., Manceau, J.C., Gaboreau, S., Pichavant, M., Audigane, P., 2018. Determination of hydrogen–water relative permeability and capillary pressure in sandstone: Application to underground hydrogen injection in sedimentary formations. Transp. Porous Media 122 (2), 333–356.

Yiotis, A.G., Psihogios, J., Kainourgiakis, M.E., Papaioannou, A., Stubos, A.K., 2007. A lattice Boltzmann study of viscous coupling effects in immiscible two-phase flow in porous media. Colloids Surf. A 300 (1–2), 35–49.

Yu, Z., Fan, L.S., 2010. Multirelaxation-time interaction-potential-based lattice Boltzmann model for two-phase flow. Phys. Rev. E 82 (4), 046708.

Yuan, P., Schaefer, L., 2006. Equations of state in a lattice Boltzmann model. Phys. Fluids 18 (4), 042101.

Zhang, Y., Bijeljic, B., Gao, Y., Goodarzi, S., Foroughi, S., Blunt, M.J., 2023. Pore-scale observations of hydrogen trapping and migration in porous rock: Demonstrating the effect of Ostwald ripening. Geophys. Res. Lett. 50 (7), e2022GL102383.

Zhang, T., Zhang, L., Zhao, Y., Zhang, R., Zhang, D., He, X., Ge, F., Wu, J., Javadpour, F., 2022. Ganglia dynamics during imbibition and drainage processes in nanoporous systems. Phys. Fluids 34 (4), 042016.

Zhao, J., Kang, Q., Yao, J., Viswanathan, H., Pawar, R., Zhang, L., Sun, H., 2018. The effect of wettability heterogeneity on relative permeability of two-phase flow in porous media: A lattice Boltzmann study. Water Resour. Res. 54 (2), 1295–1311.

Zhao, H., Ning, Z., Kang, Q., Chen, L., Zhao, T., 2017. Relative permeability of two immiscible fluids flowing through porous media determined by lattice Boltzmann method. Int. Commun. Heat Mass Transfer 85, 53–61.

Zhao, Q., Wang, Y., Chen, C., 2023. Numerical simulation of the impact of different cushion gases on underground hydrogen storage in aquifers based on an experimentally-benchmarked equation-of-state. Int. J. Hydrog. Energy.

Zhao, J., Yao, J., Li, A., Zhang, M., Zhang, L., Yang, Y., Sun, H., 2016. Simulation of microscale gas flow in heterogeneous porous media based on the lattice Boltzmann method. J. Appl. Phys. 120 (8), 084306.

Zhao, W., Zhang, Y., Xu, B., 2019. An improved pseudopotential multi-relaxation-time lattice Boltzmann model for binary droplet collision with large density ratio. Fluid Dyn. Res. 51 (2), 025510.

Zivar, D., Kumar, S., Foroozesh, J., 2021. Underground hydrogen storage: A comprehensive review. Int. J. Hydrog. Energy 46 (45), 23436–23462.